Towards retinal membrane peeling with a handheld robotic instrument

Arpita Routray

CMU-RI-TR-19-71

August 2019

Robotics Institute
Carnegie Mellon University
Pittsburgh, Pennsylvania, 15213

THESIS COMMITTEE

Cameron N. Riviere

John Michael Galeotti

Chengqian Che

Submitted in partial fulfillment of the requirements for the degree of Masters in Robotics

Contents

1 Introduction **1**

1.1 Background 2

1.1.1 Epiretinal Membrane Peeling 2

1.1.2 Robot-Assisted Retinal Surgery 3

1.1.3 Micron and Related Systems 4

1.2 Related Work 7

1.3 Clinical Goals 8

1.4 Motivation 8

1.5 Technical Contributions 9

1.6 Outline 11

2 Real Time Update of Retinal Plane **12**

2.1 Retinal Plane Update 13

2.1.1 Function Approximation 14

2.1.2 Error Calibration 14

2.1.3 Plane Update Method 16

2.1.4 Experiments 17

2.1.5 Results 18

2.2 Estimation of Points in Saline Water 21

2.2.1 Function Approximation 21

2.2.2 Error Calibration 21
2.2.3 Experiments 22
2.2.4 Results 23

3 Open-Sky Membrane Peeling with Virtual Fixtures **25**
3.1 Retinal Surface Estimation 25
3.2 Virtual Fixtures 27
3.3 Experimental Setup 29
3.4 Results 29

4 Discussion **32**

List of Figures **35**

List of Tables **37**

Bibliography **38**

Acknowledgement

I would like to thank Dr. Cameron Riviere for agreeing to advise me during my program. This work would not have been possible without his invaluable guidance. I would also like to thank Robert MacLachlan and Yuqiao Han for their crucial assistance and input during my work. I am also grateful to Dr. John Galeotti and Chengqian Che for agreeing to be on my thesis committee. I am immensely grateful to my parents, without whose support I would never have started this work.

Abstract

Vitreoretinal surgery procedures demand high precision and have to be performed with limited visualization and access. One such procedure is membrane peeling, which involves peeling of the 5-10 μm thick internal limiting membrane around macular holes. Robot-aided surgery has a lot of potential to improve the safety and accuracy of these procedures. Our goal is to develop a system for membrane peeling with the actuated handheld instrument Micron using virtual fixtures that works in-vivo. A cornerstone of many of the proposed virtual fixtures is reconstruction of the retinal surface with respect to the surgical tool, which is difficult to obtain due to the inadequacy of traditional stereo vision techniques in the intact eye. Instead, we aim to estimate the position of the retina in an intact eye by tracking a laser aiming beam interfaced with the Micron end-effector .

To move towards these goals, we develop virtual fixtures for membrane peeling and test their effectiveness with open-sky experiments in an artificial phantom. We find a significant reduction in the forces applied at the phantom during the robot-aided trials. To obtain an estimate of the retinal plane in-vivo, a structured-light technique using an aiming beam interfaced with the handheld instrument has been proposed, but it only provides a reconstruction at the start of the procedure; it cannot update it as the eye moves during surgery. We propose updating the initial estimate of the retinal plane a single point at a time, by continued detection of a laser aiming beam in each camera frame, as in the initial structured-light approach. The efficacy of this retinal plane update method is demonstrated by tracking a plane in an open-sky experiment and finding points on the plane in saline water.

Chapter 1

Introduction

Vitreoretinal microsurgery procedures involve manipulating small, delicate structures within the eye and demand high precision [1]. One such procedure is membrane peeling, during which the 5-10 μm thick internal limiting membrane (ILM) has to be removed around macular holes and requires repeated attempts by surgeons over several minutes [2]. The use of appropriate virtual fixtures in conjunction with robotic systems can improve the precision of these procedures and actualize required safeguards.

Using an active handheld manipulator called Micron [3], we develop virtual fixtures for epiretinal membrane peeling and demonstrate their effectiveness in an artificial phantom. A requirement for the success of these virtual fixtures is an accurate estimate of the position of the retina with respect to the tool tip. However, due to the complexity of the light path in the intact eye, retinal surface estimation is difficult. The algorithm described in [4] uses a structured light approach to estimate the initial position of the retina in an intact eye, but cannot be used intra-operatively in real time because it requires non-manipulative actuation of the end-effector. We thus propose a framework to track the in-plane motion of the retina during surgery.

1.1 Background

1.1.1 Epiretinal Membrane Peeling

An epiretinal membrane (ERM) is a 60μm thick avascular semitransparent membrane which can develop on the inner retinal surface. It is a common condition and studies show a prevalence of 6.0% to 11.8% in populations aged over 40 [5][6]. The prevalence of ERM is higher in eyes with diabetic retinopathy, cataract surgery, and diseases like retinal detachment and retinal vascular disease. The risk of this condition also increases significantly with age. There are several theories regarding the cause of ERM, all of which revolve around posterior vitreous detachment (PVD), which describes the separation of the vitreous from the retina [7][8]. The presence of ERM is usually asymptomatic. However, the membrane may contract over time resulting in puckering of the retina. This can lead to metamorphopsia and blurred vision. Treatment of this issue involves removal of the epiretinal membrane by peeling. To decrease chances of the condition reoccurring, the 0.5-2.5 μm thick transparent internal limiting membrane at the interface of the retina and the vitreous may also be peeled [9].

To enable better access to the retina during peeling, vitrectomy is performed wherein incisions are made in the sclera and the vitreous gel is replaced by saline water. To start peeling, first a bent tool such as a bent needle or forceps is slipped underneath a flap of the membrane. Once the membrane is lifted, peeling takes place by moving the tool in a circular motion in parallel to the retinal surface.

Membrane peeling is challenging even for experienced surgeons due to the minuscule dimensions and delicate nature of the structures being manipulated. The membrane is hard to discern and can break during peeling. Thus, it may require repeated attempts by surgeons over several minutes. This procedure is performed by inserting the tool through a port in the sclera and tool movement is restricted to four degrees of freedom. Surgeons also have to ensure that the tool does not exert excessive forces at this port, thus having to maintain a remote-centre-of motion (RCM) at this port and having to compensate for eye motion. Additionally, this pro-

cedure has to be visualized through an operating stereo microscope. Excessive forces exerted by the tool on the retina can lead to damage to the nerve fibre layer, retinal haemorrhages and changes in vision. However, the forces exerted during this procedure are often too small to be perceptible by surgeons [10][11]. Another fundamental hindrance to precise manipulation is the surgeon's involuntary hand tremor, which can translate to 100 μm peak-to-peak magnitude at the tool-tip [12].

Robotic technology has rich potential to aid vitreoretinal microsurgery procedures like peeling. Technologies that allow motion scaling, virtual fixtures to stop the tool tip from entering forbidden regions, tremor cancellation to facilitate precise positioning of the tool, force sensing, and improved visualization can improve the safety and accuracy of this procedure while reducing cognitive load on the surgeon.

1.1.2 Robot-Assisted Retinal Surgery

Similar to peeling, other vireoretinal microsurgery procedures also require surgeons to perform procedures that manipulate minute and delicate tissues in the fragile retina. For example, retinal vein cannulation involves drug delivery to retinal vessels less than 100 microns in diameter [13]. Constrained workspaces, restricted visualization, and human limitations considerably hamper the accuracy and precision with which surgeons can perform these procedures. Robotic technology can facilitate performing risky or impossible procedures by incorporating safeguards against unintentional damage to essential retinal structures, facilitating schemes that can render a surgeons' actual intended behavior at the robot end-effector with high accuracy and precision, and technologies to improve visualization. Additionally, repetitive tasks can also be automated so that surgeons can pay attention to the more demanding parts of the task.

Many robotic systems have been developed specifically for ophthalmic surgery. In the JHU Steady-Hand Robot system [14] [15], the surgical tool is simultaneously controlled by the surgeon and the robot. The system uses Fourier-domain optical coherence tomography feed-

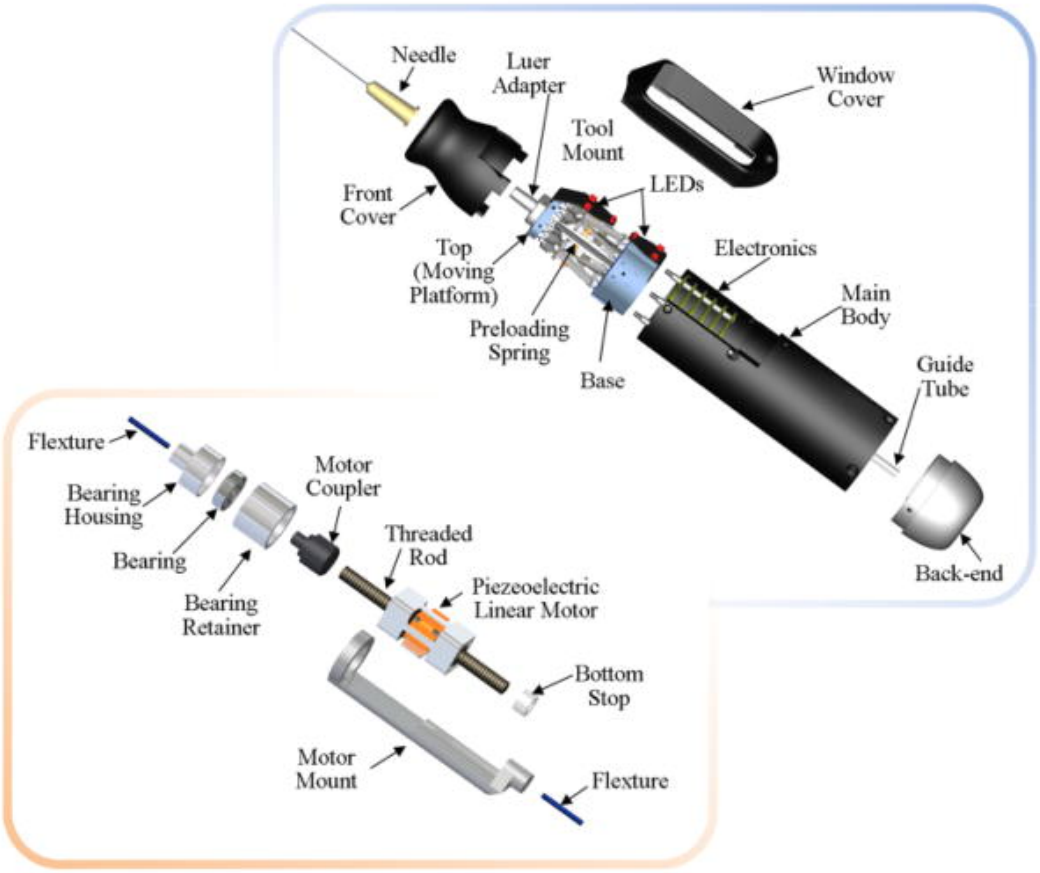

Figure 1.1: Exploded view of Micron

back for one-dimensional tremor cancellation and is equipped with a 3-DoF force sensor to facilitate force feedback. The Preceyes surgical system [16] is a master-slave system that incorporates tremor cancellation, motion scaling, better positioning, and upscaled force feedback. In [17], electromagnetically controlled wireless microbots are proposed for vitreoretinal microsurgery . An actuated handheld instrument called Micron that incorporates tremor cancellation [3] has also been developed for this purpose.

1.1.3 Micron and Related Systems

Micron is an active handheld robotic instrument for accuracy enhancement that can provide active compensation for the surgeons' physiological hand tremor [3]. The version of Micron used for this experiment is 6-DoF system actuated by a prismatic-spherical-spherical Gough

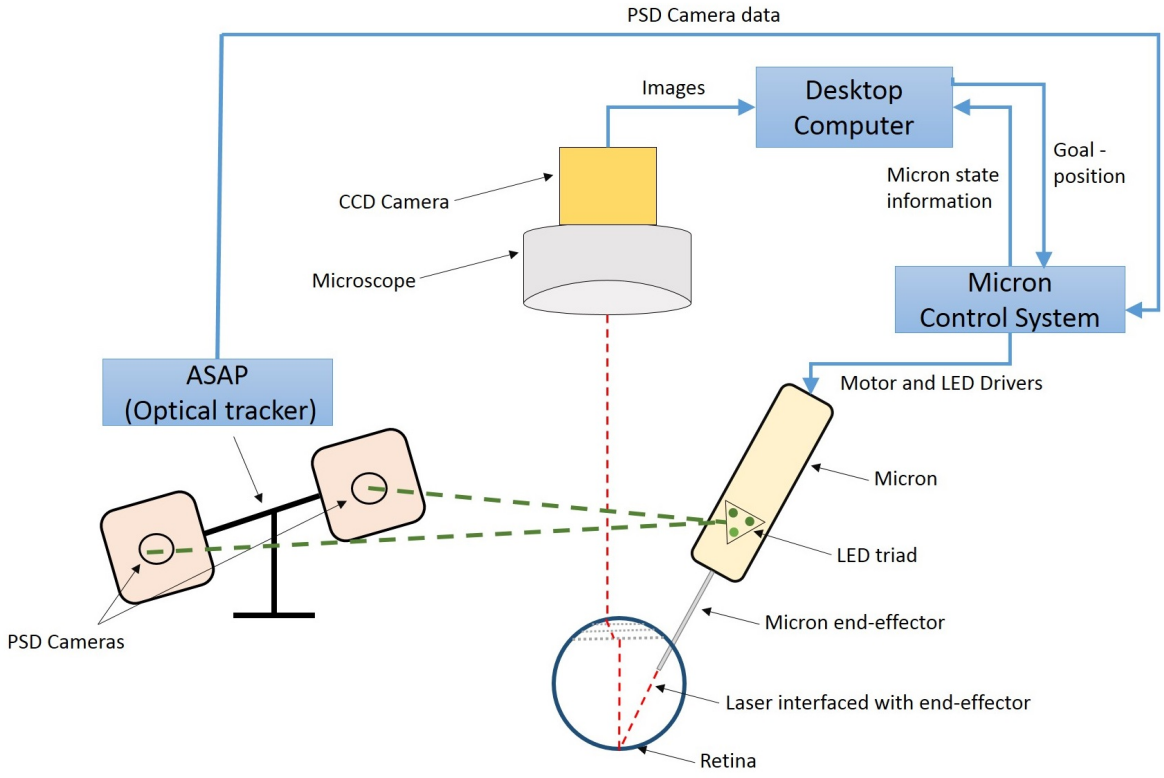

Figure 1.2: Schematic diagram showing Micron and all associated systems

Stewart platform that uses piezoelectric linear motors. Surgical tools that act as end-effectors can be attached to this platform and this end-effector has a cylindrical workspace that is 4mm in diameter and 6mm long with its null position at the centroid of the space. An exploded view of this device is shown in Figure 2.1.

The device has a set of 3 LEDs fixed to the handle, which are optically tracked by using position-sensitive detectors (PSD) in a custom built optical tracking system called 'Apparatus to Sense Accuracy of Position' (ASAP) [18] at a sampling rate of 1 kHz. The full 6DOF pose of the instrument handle in fixed global coordinates is computed by triangulating three frequency-multiplexed LEDs mounted on the instrument [18]. This position of the instrument handle is available in micrometer resolution over a region spanning 3 centimetres.

To move the Micron end-effector to any point within its workspace, the desired link-lengths of the Gough-Stewart platform are computed using inverse kinematics and control takes place

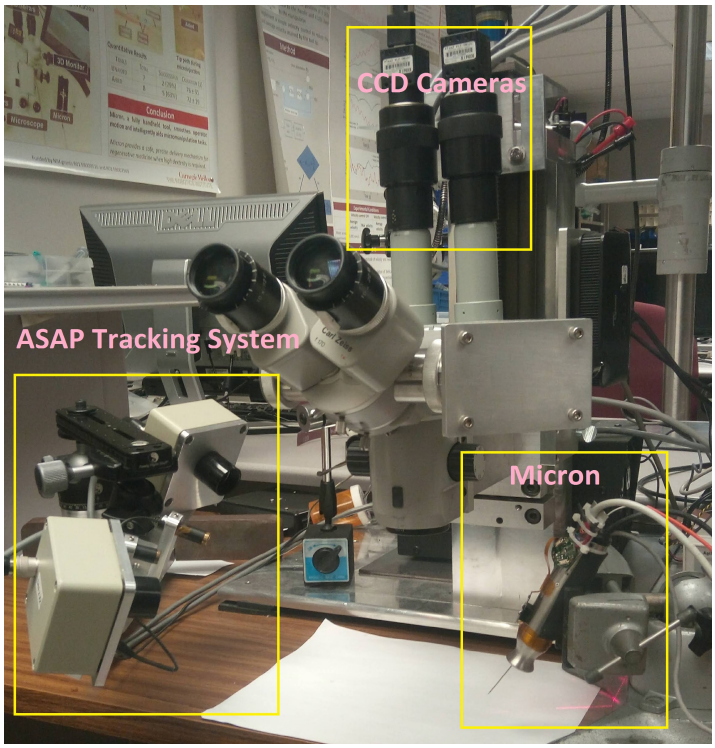

Figure 1.3: Micron system setup, showing Micron handheld vitreoretinal surgical instrument, ASAP optical tracker, stereo operating microscope, and cameras.

in link-space. When all the links of the Gough-Stewart platform are at their zero positions, the resulting position of the Micron tool-tip is termed as its null position. The position where the Micron tool-tip is commanded to move to is termed its goal position.

The vision system comprises of 2 CCD cameras mounted on an operating microscope as shown in Figure 1.3. All experiments are conducted under the microscope and in full view of the two cameras. The cameras are connected to a desktop PC, which handles image processing. The PC is used to receive real-time information about the status of Micron and can also send goal positions to its control system.

In addition to tremor cancellation, Micron can also be used to actualize a number of virtual fixtures and other desired behaviors to aid ophthalmic surgery procedures [19][20][21]. For many of these virtual fixtures and behaviors, an accurate position of the retina with respect to the Micron tool-tip is required. As traditional stereo reconstruction does not work due the

complexity of the light path in the intact eye (Figure 1.4), the retina position is obtained by tracking via the cameras a laser aiming-beam interfaced with Micron. A schematic diagram of the entire system is shown in Figure 1.2.

1.2 Related Work

Many experiments have been carried out that demonstrate the effectiveness and potential of robotic systems in aiding membrane peeling. In [22], membrane peeling experiments are carried out using the cooperatively controlled Steady-Hand Eye robot. A 3-DoF force sensing instrument that has submillinewton accuracy is attached to the robot tool-holder and provides information about the force exerted by the subject during the experiment. The applied force during the experiment is relayed to the subject using audio that appropriately alerts the user if they exceed a force threshold. Open-sky experiments are carried out in artificial and biological phantoms by a novice. Experiments during which the subject is presented with audio-based force feedback show lower mean forces and lower maximum forces compared to experiments where there is no feedback.

In [16], an in-human study on the viability of robot-aided vitreoretinal surgery is conducted using the master-slave Preceyes surgical system. Results do not show any difference in retinal microtrauma in the aided and unaided cases. However, time taken for peeling using the robotic system is higher.

In [23], a 3-DoF version of Micron [24] is used to aid Membrane Peeling in an artificial phantom with the help of multi-part vision-based virtual fixtures. In this membrane peeling system, when the Micron tool-tip is within 50 μm of the estimated retinal surface, motion is scaled perpendicular to the surface. The tool-tip is also not allowed to move beyond a hard-stop employed at 50 μm beneath the estimated retinal surface. Additionally, tool-tip velocities are capped at 100 μm/s. The retinal surface is estimated using stereo reconstruction. The efficacy of the proposed system of virtual fixtures is validated in an artificial phantom and results show a 73.6% decrease in downward engaging force and a 42.9% decrease in

upward peeling force.

1.3 Clinical Goals

Our goal is to develop a system for membrane peeling using the handheld instrument Micron that works in-vivo. In this system, membrane peeling will be aided by customized virtual fixtures that depend on the position of the surgical tool-tip with respect to the retina. These virtual fixtures will be designed to help the surgeon lift and peel the membrane while preventing penetration of the retina, avoiding breaking of the membrane during peeling, and minimizing applied force to the retina. The position of the retina with respect to the Micron tool-tip will be estimated in-vivo by tracking an aiming beam interfaced with this surgical tool.

1.4 Motivation

Membrane Peeling is a challenging task for surgeons due to the issues described in sections 1.1.2 and 1.1.1. Although experiments involving Membrane Peeling aided by a 3-DoF version of Micron have been carried out in [23], this previous version of Micron only had a workspace of 1x1x0.5 mm. Moreover, the experiments were open-sky and used stereo to estimate the phantom surface. The current version of Micron has a larger workspace that is 4mm in diameter around its tool-tip's null position. Thus, we would like to take advantage of this larger workspace to implement virtual fixtures to aid this challenging procedure.

For the success of the proposed virtual fixtures, an accurate estimate of the position of the retina with respect to the tool tip is required. Retinal surface estimation is difficult because traditional stereo surface reconstruction methods cannot be used successfully. This is because, during surgery, the optical path involves the cornea, the lens, saline, and also a BIOM (Binocular Indirect OphthalmoMicroscope) lens 1.4. Due to the shortcomings of traditional reconstruction methods in the intact eye, many authors have proposed alternative methods of registering the position of the retina to the surgical tool tip. In [25], the authors use the dis-

tance between the tool tip and its shadow in the acquired images to detect proximity, but the method does not provide the exact distance of the tool tip from the retina. A focus-based 3D localization method using the Navarro schematic eye is developed in [26], but the localization error remains few hundred microns.

In all of the above methods, the tool tip is localized using visual feedback. On the other hand, the tool tip of the handheld robot Micron can be tracked at all times using the optical tracking system ASAP. Taking advantage of this information, a new method for retinal surface reconstruction was introduced in [4] using structured light applied by a laser aiming beam. This method involves moving the Micron tool tip in a circular trajectory, which is practical only before beginning a surgical procedure, and not during it. Thus, it can only provide an initial estimate of the retinal plane and is not suitable for intraoperative updates. During vitreoretinal surgery the patient is sedated rather than anesthetized, and movements of the eye are common [27]. To account for movement of the retinal surface, we propose a framework that updates the estimate of the retinal plane in real time. Real-time estimation of the retinal plane will also help in testing the efficacy of these fixtures in live animals where the retinal surface may move over time.

1.5 Technical Contributions

We develop and test virtual fixtures for epiretinal membrane peeling in an artificial phantom using the current 6-DoF version of Micron. Instead of stereo, we use the structured light method described in [4] to estimate the phantom surface. To determine the efficacy of our virtual fixtures, we analyse the forces during aided and unaided trials.

Membrane peeling in an intact eye consists of three steps: engaging, wherein the bent tool is inserted beneath the membrane, lifting of the membrane, and peeling. Engaging and lifting occur close to the retina, whereas during peeling, the tool-tip is farther away. To ensure repeatability, we demonstrate the efficacy of our virtual fixtures in an artificial phantom. Removal of this phantom membrane does not require the tool-tip to move far from the surface

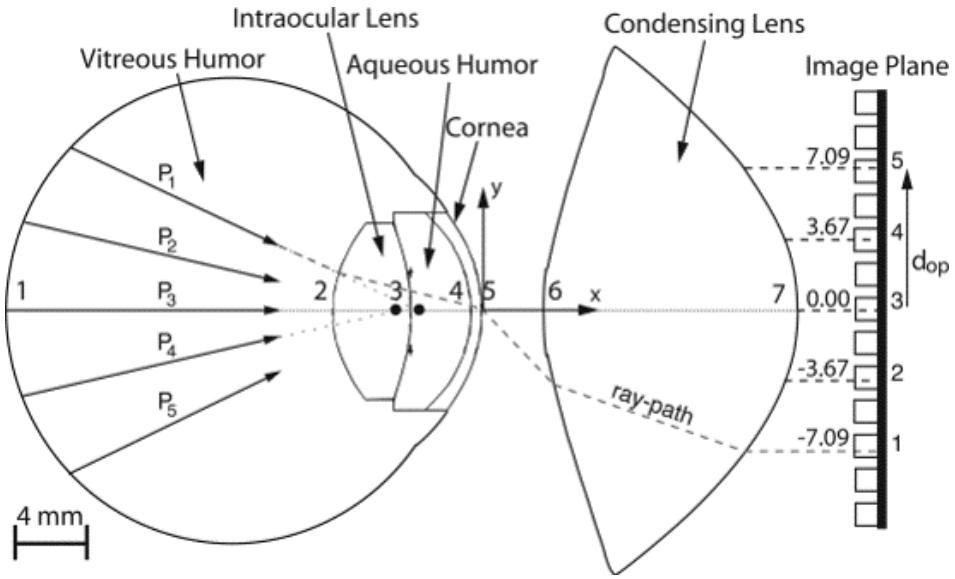

Figure 1.4: Schematic diagram showing ray paths (P_1 to P_5) in the eye [28]. The ray paths, also called "isopixel curves", are shown at fixed steps of 3.5 mm along with their correspondences to pixel distances d_{op} from the optical axis.

and mostly requires a lifting motion. Thus, although the virtual fixtures are designed to aid every step of the membrane peeling process, experiments with the phantoms demonstrate the efficacy of the engaging and lifting steps.

We also propose a framework for updating the estimated retinal plane in real-time by tracking a laser interfaced with Micron in the camera images. This framework consists of two parts. In the first part, using information from the camera images, the point at which the Micron laser intersects the retinal plane is determined. This is done by estimating a function that maps between 3D world coordinates to image coordinates using Micron tool-tip data, and using the resultant mapping and information about the laser in the camera images, we estimate the point at which the aiming beam intersects the retinal surface.

There are many sources of errors that can hamper the process of estimating the mapping function and computing the point at which the laser intersects the retina. We identify potential error sources and also present a method to calibrate for these errors. We carry out an experiment that demonstrates the efficacy of combining the function estimation and error

calibration techniques to find points on a phantom plane submerged in saline water.

The second part of the retinal plane update framework uses this information about the estimated point on the retinal plane determined from each incoming camera frame to update the current retinal plane estimate. We demonstrate the feasibility of this second part by tracking a phantom plane over 120 seconds in an open-sky experiment.

1.6 Outline

In chapter 2, we first describe our overall framework for updating the retinal plane in real time by tracking the laser interfaced with Micron in the camera images. Following this, we describe in detail the first part of our framework in which the retinal plane is updated one point at a time, wherein each point is obtained using information from an incoming camera frame. We then describe the setup and results from an experiment that tracks a phantom plane over 120 seconds to determine the feasibility of the proposed plane update method. Finally, we demonstrate the efficacy of determine points on a phantom plane submerged in saline water.

In chapter 3, we demonstrate the effectiveness of virtual fixtures for membrane peeling using the current version of Micron. First, we describe the structured light method that is used to estimate the phantom plane. Following this, we describe the virtual fixtures used. We then describe our experimental setup and summarize our results. Finally, in chapter 4, we summarize our work and discuss future directions.

Chapter 2

Real Time Update of Retinal Plane

An accurate position of the retinal plane in the ASAP world coordinate system is required for the virtual fixtures for membrane peeling described in section 3.2. An initial approximation to the retinal plane can be found using [4]. In this method, a laser interfaced with the micron end-effector is moved in a circular trajectory and the projective geometry of the resulting ellipse is get an estimate of the plane. This method is described in more detail in Section 3.1. However, this method cannot be use intra-operatively. Thus, we propose a framework that, given an initial estimation of the plane, can update the retinal plane in real-time.

In addition to the complex optics of the intact eye that make traditional techniques of surface reconstruction using stereo ineffective, the magnified retina suffers from a lack of texture and sparsity of keypoints. On the other hand, the centre of a laser interfaced with Micron is easily detectable in the camera images. Although lasers are not normally incorporated into vitreoretinal instruments except for theurapeutic laser instruments, in principle it is possible to do so. We have integrated a laser with a tool for membrane peeling and are currently working on incorporating aiming beams into the shaft of other instruments.

Thus, we propose to use the beam information from the camera images to find the intersection point of the laser and the camera and then update the current retinal plane taking this infor-

mation into account. This proposed framework consists of two parts. The first part involves finding the point at which the laser intersects the retinal plane. The second part consists of updating the retinal plane using this point.

Our algorithm for estimation of a point on the retinal plane again consists of two parts. The first part involves function approximation, wherein a function that maps 3D ASAP world coordinates to image coordinates is estimated. The Micron tool-tip can be detected in camera images. Thus, at any instant, we have the coordinates of the Micron tool-tip in the ASAP-world coordinate system, along with its image coordinates. We propose to use this data to estimate a function that relates points in the world coordinate system to points in the image coordinate system. Normally, in homogeneous media, camera matrices are used to linearly relate homogeneous coordinates in the world coordinate system to the image coordinate system. We show that camera matrices are also a good approximation in the case where the retinal plane is in saline water, provided we only use the Micron tool-tip data when it is within a few millimetres of the initially estimated plane.

The second part of our algorithm for retinal plane point estimation involves error calibration. Due to inaccuracies arising from many sources, like error in detecting the precise location of the laser centre in the images, or error in the tool-tip length, the laser point found in 3D ASAP coordinates may be erroneous. Thus, we propose to use laser data from a known initial plane to calibrate these errors. An error calibration method that calibrates the errors in laser centres is described in section 2.1.2 and is used in the open-sky plane tracking experiment. This error calibration method is extended in section 2.2.2 to calibrate an additional depth error.

2.1 Retinal Plane Update

We first demonstrate the feasibility of updating the retinal plane one point at a time, wherein each point is derived using information from a camera image frame. We do so by tracking a phantom plane over a period of 120 seconds in an open sky experiment. At any point of time t, we first estimate the point at which the laser beam interfaced with Micron intersects the

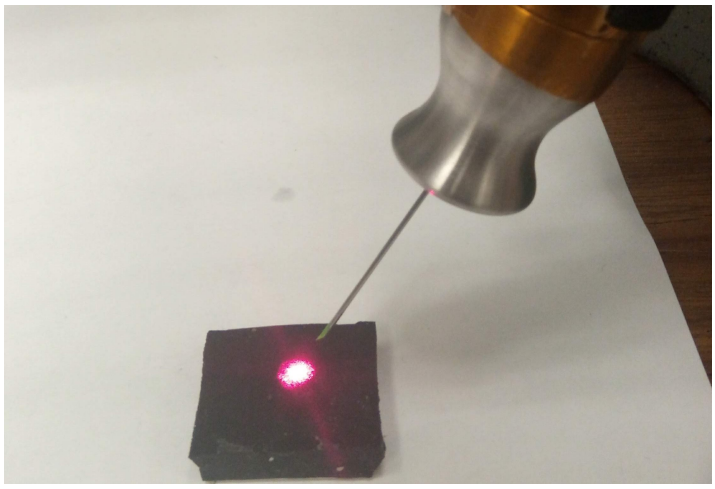

Figure 2.1: Laser interfaced with the Micron end-effector.

retinal surface in 3D ASAP coordinates. Given the noisy linearly triangulated beam points, we then outline the method to update the estimate of a point on the plane and the plane normal. Π_t is used to denote the estimated plane at the instant t. For this study, the initial estimate of the plane at time $t = 0$, Π_0, is assumed as given.

2.1.1 Function Approximation

We use stereo vision to triangulate the position of a single point on the retinal plane. To do so, we first calibrate each camera's 2D image coordinate system to the 3D ASAP coordinate system. To get correspondences between the camera coordinates and ASAP coordinates, the Micron tool tip is detected in each camera and its 3D position in ASAP coordinates is recorded simultaneously. Using these correspondences, the projection matrices of both cameras are computed using DLT and RANSAC [23].

2.1.2 Error Calibration

In order to optimize the speed of our algorithm, an initial approximation of the center of the laser beam in the left and right camera images, p_{l0}, and p_{r0} is computed using simple thresholding operations. However, as the beam appears diffuse under the microscope, this position may not be the exact point at which the laser beam intersects the retinal surface. We

assume that the actual position of the laser beam differs from the initial approximation in the left and right images by constant error offsets, ρ_l and ρ_r, respectively. Thus, if p_l and p_r be the actual positions at which the laser beam intersects the retinal surface, we have

$$\begin{aligned} p_l &= p_{l0} + \rho_l \\ p_r &= p_{r0} + \rho_r \end{aligned} \tag{2.1}$$

For a set of planes Π_i and the corresponding beam locations $p_{l,i}$ and $p_{r,i}$, we define the following terms:

$T(p_{l,i}, p_{r,i})$, the triangulated 3D point using $p_{l,i}$, $p_{r,i}$

d_i, signed distance between $T(p_{l,i}, p_{r,i})$ and the plane Π_i

$M(d_i)$, median over all d_i

$\mu_x(|d_i|)$, x% trimmed mean over all $|d_i|$

The offsets ρ_l andρ_r are then computed by minimization of the following objective function:

$$F(\rho_l, \rho_r) = 0.5\big|M(d_i)\big| + 0.5\big|\mu_5(|d_i|)\big| + \sqrt{\rho_l^2 + \rho_r^2} \tag{2.2}$$

Minimization of the first term ensures that the triangulated beam points are distributed evenly above and below the true retinal plane, thus avoiding any offsets during plane estimation. Minimization of the second term reduces the distances of the triangulated beam points from the true retinal plane. The third term is simply used for regularization. A separate dataset spanning 100 seconds is used to compute ρ_l andρ_r by optimizing (2.2). Using this method, we get ρ_l = [1.12, 1.70] pixels and ρ_r = [-2.99, 0.69] pixels.

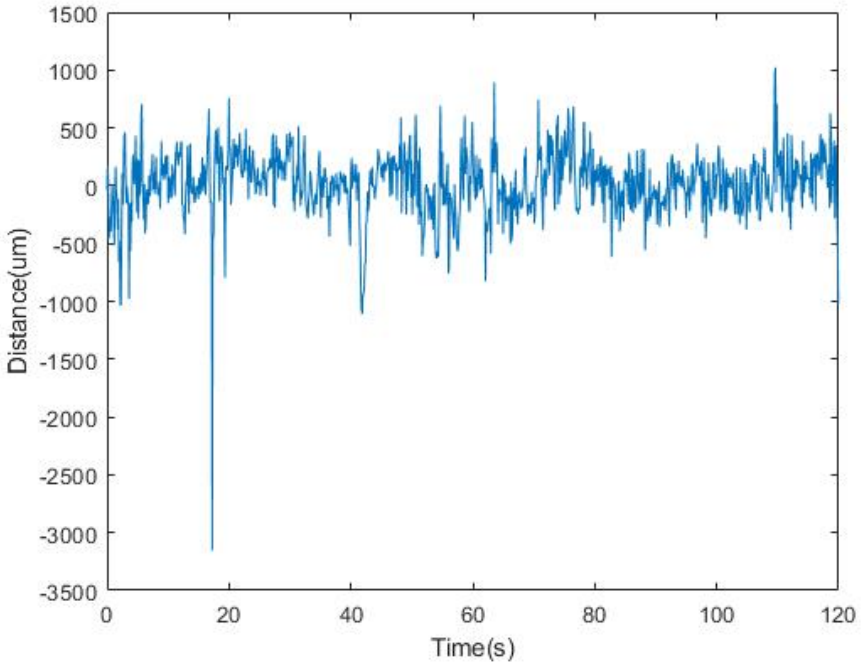

Figure 2.2: Distances of the estimated position of the intersection of the laser beam and the retinal surface from the true phantom plane during the surface tracking experiment. The plot demonstrates that the triangulated beam points are noisy, and hence should be filtered.

2.1.3 Plane Update Method

Surface Point Update

The triangulated beam points computed in section 2.1.2 are noisy. In order to filter out high-frequency noise components, we use a moving average filter, and the estimate of a point on the plane is computed as a weighted sum of the previous estimate and the latest filtered beam point. If P_t be the estimate of a point on the plane at time t, then

$$P_t = w_p \sum_{i=t-k_p}^{t} T(p_{l,i}, p_{r,i}) + (1 - w_p) P_{t-1} \tag{2.3}$$

where the parameters k_p and w_p are the filter window size and the weight corresponding to the latest point update, respectively.

Surface Normal Update

An intermediate value of the plane normal, n'_t, is computed by fitting a plane to the last m_n triangulated beam points, such that all points are at least a distance Δ_n away from from each other. The estimate of the plane normal is computed as a weighted sum of the previous estimate and n'_t. If n_t be the estimate of a point on the plane at time t, then

$$n_t = w_n n'_t + (1 - w_n) n_{t-1} \tag{2.4}$$

where the parameter w_n is the weight corresponding to the latest normal update.

Noisy and Missing Points

If the distance between $T(p_{l,t}, p_{r,t})$ and the estimated plane Π_{t-1} is greater than a threshold Δ_d, or if the laser beam is not detected in the camera images, we set $p_{l,t} = p_{l,t-1}$ and $p_{r,t} = p_{r,t-1}$. P_t and n_t are then computed as usual using (2.3) and (2.4). This ensures that the estimated plane is not stagnant during such instances and keeps moving incrementally towards the last position of the triangulated beam point. Hence, once we again get a usable value of $T(p_{l,t}, p_{r,t})$; the plane update resumes with a reduced lag.

2.1.4 Experiments

For update of the plane normals, we use the past $m_n = 7$ points, an update weight of $w_n = 0.015$, and a minimum distance between fitted points, $\Delta_n = 50\mu m$. For update of the points on the plane, we use a filter window size of $k_p = 4$ and an update weight of $w_p = 0.2$. The threshold for classifying a point as noise, Δ_d is 5mm. All parameters remain constant throughout the experiment; their values were selected via trial and error.

An initial estimate of the phantom plane is provided at $t = 0$, following which we track changes in this plane over a period of 120 seconds. Over this time period, the plane is rotated and translated manually. As shown in Figure 2.3, four cross-shaped fiducial markers are placed on the surface to be estimated. Ground truth is computed by detecting the centers

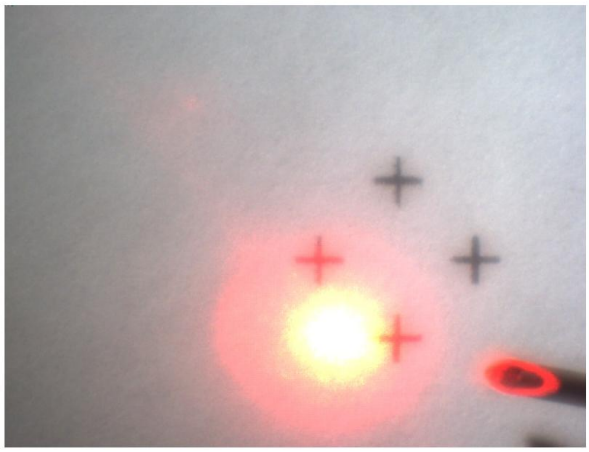

Figure 2.3: Fiducials used for estimation of the true plane during the surface tracking experiment.

of the fiducials, triangulating to obtain their positions in 3D coordinates, and then fitting a plane to these points. This method to obtain ground truth yields reliable estimates of the true phantom plane during the experiment. In frames where the fiducial markers are not visible from the camera due to sudden movements, the ground truth plane is computed by interpolation.

As the motion of the phantom plane is rapid and also involves hand tremor, the ground truth data is noisy as seen in Figure 2.4. Also, in order to track the rapid motion of this plane, we only use a filter window size of $k_p = 4$. For in-vivo experiments, a larger value of k_p may be used for less noisy estimates.

2.1.5 Results

Although the optimized offsets $\rho_l = [1.12, 1.70]$ pixels and $\rho_r = [-2.99, 0.69]$ pixels are quite small, the median signed distance $\left|M(d_i)\right|$ and the trimmed mean distance $\mu_5(|d_i|)$, as defined in section 2.1.2, reduce by 95.75% and 64.36% in the test dataset.

During the tracking period, we measure the displacement of the updated plane along the ASAP coordinate system's z axis with respect to a stationary point on the initial plane, and

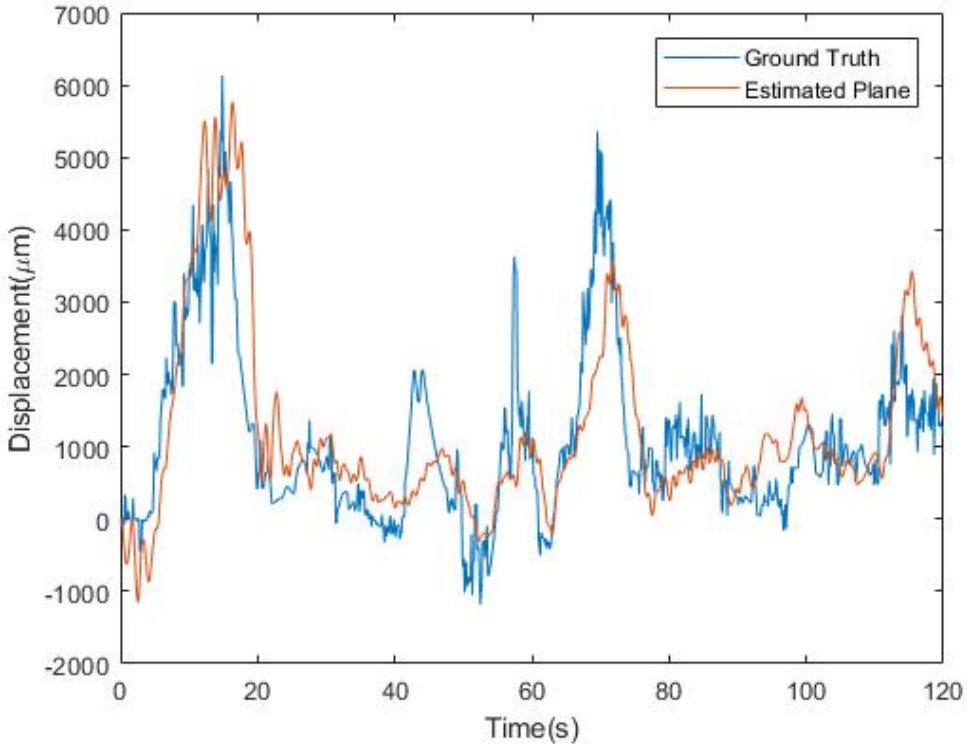

Figure 2.4: Plane displacement along z axis over the surface tracking period. The displacement in the z axis is computed with respect to a stationary point on the initial plane.

find that movement along this axis is compensated by 44.43%. As the plane normal is almost perpendicular to the ASAP system's x and y axes, we do not measure displacement along these other directions. Translations of the estimated plane and the true plane along the z axis over the tracking period is shown in Figure 2.4. We also measure the angles of the estimated and true plane normals with respect to the ASAP system's x, y, and z axes during this period. These values are plotted over time in Figure 2.5 and we observe that for the most part, the estimated normal follows the trends of the true plane normal.

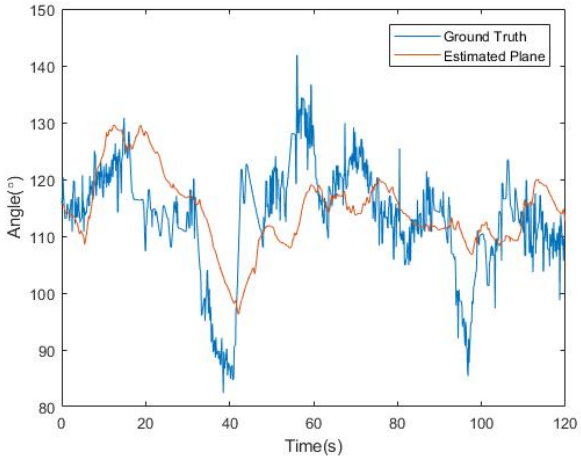

(a) Angle between plane normal and x axis

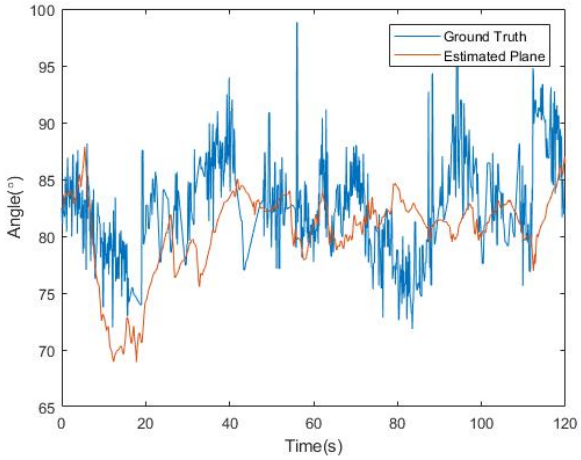

(b) Angle between plane normal and y axis

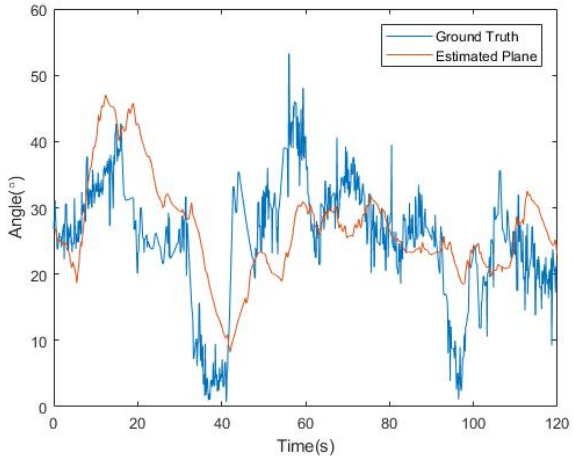

(c) Angle between plane normal and z axis

Figure 2.5: Angles of the estimated and true plane normals from the x,y, and z axes during the surface tracking experiment.

2.2 Estimation of Points in Saline Water

2.2.1 Function Approximation

For points in saline water, we also approximate the tips using camera matrices that linearly relate the homogeneous coordinates of the Micron tip in the ASAP system to the homogeneous coordinates of the tip in the image coordinate system. As in the previous case, we detect the Micron tip in the camera images, match the image coordinates of the tip to the 3D coordinates of the tip as detected by ASAP, and then use Direct Linear Transformation to compute the camera matrices. However, in this case, we only record and use the Micron tool-tip data when the tip is within a few millimetres of the initially computed retinal plane. We collect 1000 such corresponding image and ASAP tool-tip data and use them to compute camera matrices. The median re-projection error, where the re-projected 3D tip coordinates are obtained by linear triangulation, is only 189 microns. Moreover, the linear correlation coefficient between the re-projection error and the distance of the tool-tip to the plane is only -0.0066, indicating that the re-projection error is reasonably independent of the depth of the tool tip in the saline water (Figure 2.6) . As light travels though heterogeneous media in this case, these camera matrices cannot be accurately decomposed into intrinsic and extrinsic matrices that give us information about the cameras' rotation and translation with respect to the world coordinate system and each other. However, they are effective purely as functions that map the the 3D world coordinate system to the image coordinate system

2.2.2 Error Calibration

In addition to the calibration of the laser centres described in Section 2.1.2, we propose a depth offset for the linearly triangulated laser points. The depth offset can arise due to the fact that the camera matrices are computed using the Micron tool-tip data only in the area above the retinal plane. Additionally, the tool tip length of Micron may be inaccurate, leading to inaccurate world coordinates of the tool-tip. Thus is n_i be the normal to the initially computed

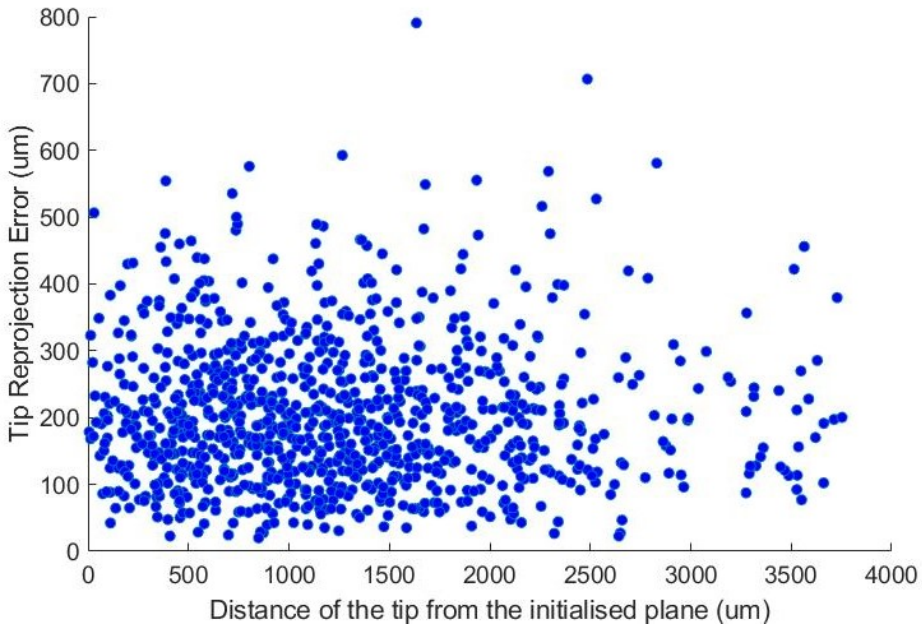

Figure 2.6: The tip reprojection error plotted against the distance of the tip from the initialized plane, which is a measure of the depth of the tip in the saline water.

plane, ρ_d be the depth offset, then

$$P = T(p_l, p_r) + \rho_d n_i \tag{2.5}$$

For error calibration in saline water we use two separate datasets. The first dataset is used to compute the laser offsets and are found to be to ρ_l = [1.78, 1.06] pixels and ρ_r =[=-0.72 ,-0.94] pixels. In the second dataset, the linearly triangulated beam points are computed by taking the laser offsets into account. ρ_d is then computed as the median of the distances of the second dataset's triangulated beam points from the actual surface. The value of ρ_d computed for the case of saline water is -53.43 microns.

2.2.3 Experiments

We place a phantom plane in saline water and estimate its position using [4]. After this, we move the laser interfaced with Micron across the surface and record the positions of the laser

centres in the camera images. We then compute the 3D laser position on the retinal surface using our described algorithm for 600 points.

2.2.4 Results

The signed distances of the computed 3D laser points from the actual retinal plane are summarized in Table 2.1. We see, the distances of the laser beam points computed using error calibration of both laser and depth offset has the smallest median signed distance and and also the smallest mean and standard deviation of the absolute distances.

	No offset	Laser Offset	Laser and Depth offset
Median d	-240.1794	91.6050	38.1662
Mean $\|d\|$	246.8292	126.47	109.240
Std. Dev. of $\|d\|$	129	93	77.96

Table 2.1: Table summarizing the signed distances d in microns of the computed 3D Laser points from the actual phantom plane with different error calibrations

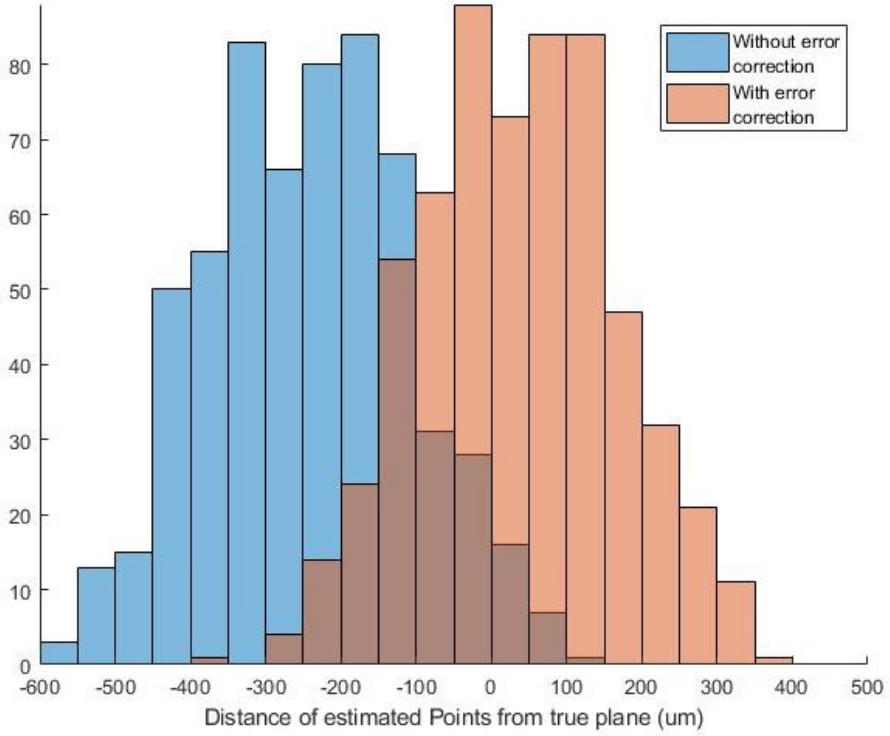

Figure 2.7: Histograms of the signed distances of the linearly triangulated laser points from the phantom plane with, and without error calibration

Chapter 3

Open-Sky Membrane Peeling with Virtual Fixtures

Similar to the fixtures described in [23], to robotically assist the process of epiretinal membrane peeling, we propose three different schemes. The first is motion scaling, wherein motion perpendicular to the estimated retinal plane is scaled when the tool-tip is within a certain distance of the retina. Secondly, we employ a hard stop which does not allow the tool-tip to penetrate below a certain distance in the estimated plane. Lastly, we employ velocity limiting at the micron tool-tip. Experiments on an artificial phantom demonstrate the effectiveness of these fixtures in reducing the applied forces to the retina while engaging and lifting the membrane.

3.1 Retinal Surface Estimation

We use the structured light method described in [4] to get an estimate of the retinal surface. In this method, the retinal surface is estimated by scanning a laser interfaced with micron in a circular trajectory, which projects an ellipse on to the retinal plane as shown in Figure 3.1. The shape and orientation of the ellipse determine the position of the retinal plane in the

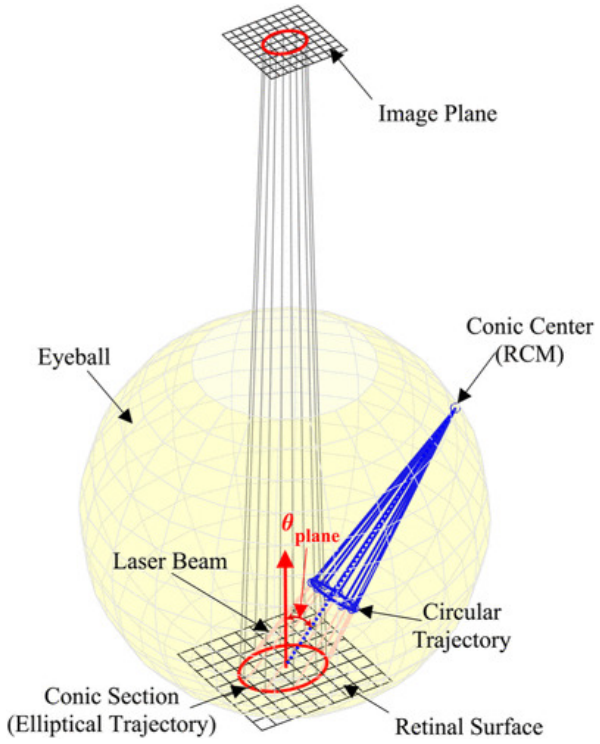

Figure 3.1: Scanning a laser interfaced with the micron end effector in a circle results in an ellipse projected onto the the retinal surface

ASAP coordinate system.

If m_a is The length of the major axis of the ellipse, and m_b is the length of the minor axis in image coordinates, the aspect ratio of the ellipse is given by:

$$\gamma = \frac{m_b}{m_a} \tag{3.1}$$

When the Micron tool tip traces out a circle, the laser line traces out a cone whose centre at the tool RCM (Fogure 3.1). If r be the radius of the circle that is traced out, and h_{rcm} the distance from the tool RCM to the tool tip, then the opening angle of the cone is given by:

$$\theta_c = \arctan(\frac{r}{h_{rcm}}) \tag{3.2}$$

The angle of the plane normal to the cone axis , where the cone axis is the line joining the

cone centre to the centre of the traced circle, is given by:

$$\theta_p = \arcsin \frac{\sqrt{1-\gamma^2}}{1+\tan {\theta_c}^2} \tag{3.3}$$

If s_{cam} be the scale factor of the image, the distance of the the plane from the cone centre along the axis of the cone is given by:

$$d_{plane} = m_a s_{cam} \cos\theta_p \frac{(1-\tan^2\theta_p \tan^2\theta_c)}{\tan\theta_c} \tag{3.4}$$

Thus, if P_{rcm} be the conce centre, and v_{cone} be the unit vector along the cone axis, a point on the plane is given by:

$$P_{plane} = P_{rcm} - d_{plane} v_{cone} \tag{3.5}$$

Although these equations uniquely find a point on the plane P_{plane}, the computed plane normal is not unique, as only the angle of the plane normal to the cone axis is given. However, the angles of each point on the re-projected ellipse to the ellipse major axis varies depending on the orientation of the plane normal. The true normal is found using an optimization that matches these angles from the re-projected ellipse to the actual angles in the image ellipse.

3.2 Virtual Fixtures

In addition to the tremor cancellation at the Micron tool tip, we employ two kinds of virtual fixtures that aid in the process of membrane peeling. First, when the distance of the Micron end-effector to the estimated retinal is less than a limit D_m, motion is scaled perpendicular to this plane. This will aid in more precise positioning of the tool tip for engaging and lifting the membrane. Secondly, we also employ a hard stop at a distance D_h below the estimated plane. In other words, we do not allow the Micron tool tip to penetrate the estimated plane below D_h. This limits the downwards force that is applied to the retina during the procedure.

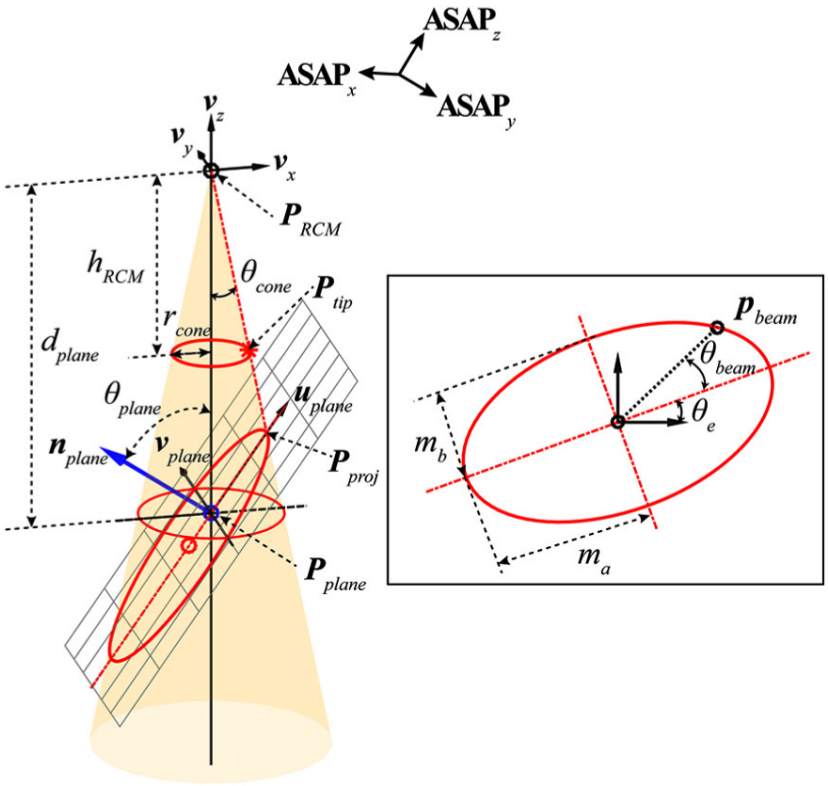

Figure 3.2: Variables used in the structured light method

Motion Scaling

When the null position of the Micron end-effector is within the motion scaling zone, motion perpendicular to the estimated retinal plane is scaled by factor of s. In particular, if the tool-tip's null position P_{null} is a distance d_{null} away from the estimated plane, and d_{null} is less than D_m, the goal position for that instant is computed using the following sets of equations:

$$\begin{aligned} d_{goal} &= D_m - \frac{D_m - d_{null}}{s} \\ P_{goal} &= P_{null} - (D_m - d_{goal})n_p \end{aligned} \tag{3.6}$$

Here P_{goal} is the computed goal position, d_goal is the distance of the computed goal position from the estimated retinal plane, and n_p is the estimated plane normal.

Hard Stop

When the distance of the motion scaled Micron goal position from the estimated retinal plane is below D_h, we compute a new goal position that ensures that the micron end-effector does not go below the hard stop D_h. In this case:

$$P_{goal} = P_{null} - D_h n_p \tag{3.7}$$

Velocity Limiting

In addition to virtual fixtures, we employ velocity limiting control that limits velocity at the Micron tool tip to 1mm/s. As demonstrated in [29], this leads to a significant decrease in the tool tip velocities during peeling experiments. This can reduce upward forces applied to the retina and prevent tearing of the membrane during peeling.

3.3 Experimental Setup

We use an artificial phantom for our membrane peeling experiments which consists of a circle of a 0.125 inch plastic film on a sticky Sorbothane rubber bad. The rubber pad is mounted on a load cell that can measure unidirectional force. Each rubber pad consists of 9 such phantoms, which aids task repetition. The films are peeled from the rubber using a needle with a slightly bent tip. We collect data for a total of 16 trials performed by a novice. These trials are divided equally into trials where the peeling task is aided and unaided by Micron.
For the virtual fixtures, we set the the motion scaling zone at $D_m = 350\mu m$ above the estimated retinal plane and the hard stop at $D_h = -50\mu m$

3.4 Results

We analyze two types of force data. The first is the mean maximum engaging force, which is the mean of the maximum downwards force during each trial. The second is the mean

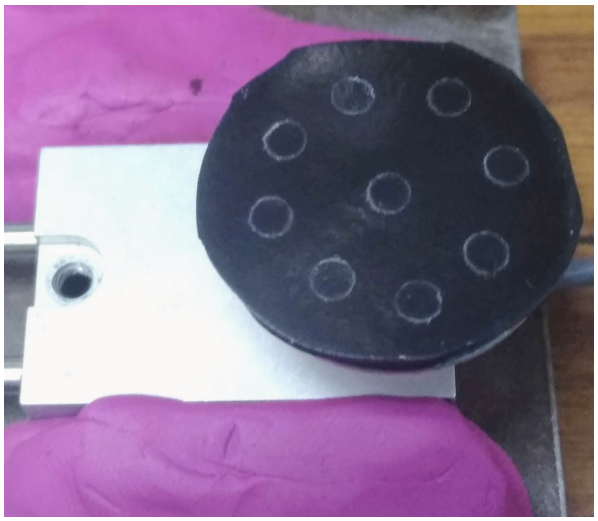

Figure 3.3: Phantom used for the membrane peeling experiment

maximum peeling force, which is the mean of the maximum upwards force during each trial. The mean maximum engaging force during unaided trials was 49.5 μN. On the other hand, the mean maximum engaging force during aided trials was 27.96 μN, which is a decrease of 43.49%. The mean maximum peeling force during unaided trials was 23.8 μN while the mean maximum engaging force during an aided trials was 13.40 μN, which is a decrease of 43.70%. Distances of the tip's null position and actual position during an aided and unaided trial are plotted in figure 3.4. In the aided trial, we observe that the tip does not go below the hard stop. On the other hand, in the unaided trial, the tip goes below the hard stop multiple times and the subject is finally able to lift the phantom membrane after several attempts.

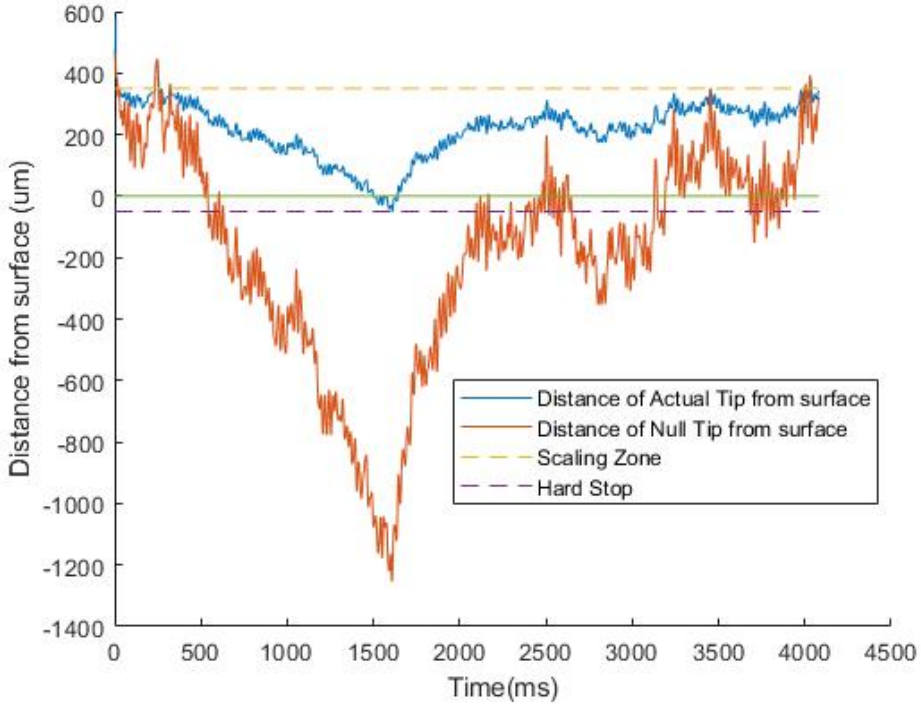

(a) Aided trial

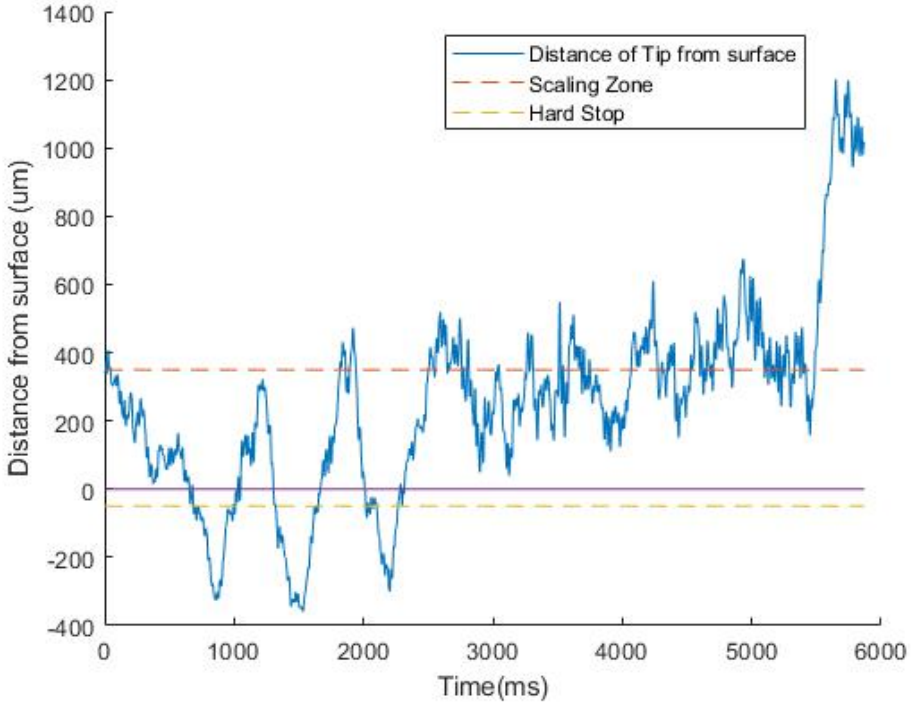

(b) Unaided trial

Figure 3.4: Distance of the actual and null tip positions from the estimated retinal surface during trial.

Chapter 4

Discussion

In this thesis, we proposed an algorithm for updating the retinal plane using noisy aiming beam samples, where only one new point is obtained from each incoming camera frame. We demonstrated the general feasibility of the method by tracking a plane in an open-sky experiment using printed fiducial markers as ground truth. We found that our method is able to track changes in the retinal plane in a stable manner, even when the plane is displaced by several millimeters. We also proposed an algorithm that combined function approximation using Micron Tool-tip data and error calibration to compute the position at which the aiming beam intersected the retinal plane. The efficacy of the algorithm was demonstrated by computing the position of points on the retinal plane in saline water and the mean distance of the estimated plane points from the actual plane was found to be only 109.24 microns.

Motion of the retinal plane perpendicular to the plane normal does not change its geometrical position in space with respect to the surgical tool tip, and hence cannot be tracked by this algorithm. However, Braun et al. have presented techniques for vision-based intraoperative tracking of retinal vasculature, which can perform this function [30]. Future work will involve combining these algorithms to tracking movements of the retinal surface in six degrees of freedom. Additionally, although camera matrices were sufficient to approximate the function that maps world coordinates to image coordinates in saline water, new functions and error

calibration methods may be required to estimate the position of points on the retinal plane in an intact eye. We also would like to investigate algorithms for online function approximation and error calibration, which would enable us to approximate the retinal plane even with motion of the cameras mounted on the microscope or the ASAP coordinate system. For the surface-tracking experiment conducted in section 2.1.3, the parameters used were constant and were selected via trial and error. Although this demonstrated the general feasibility of our method, future work will involve more systematic tuning of these parameters in order to improve the accuracy of the plane update and the lag that is visible in Fig. 2.4.

Application of the proposed plane update technique presupposes the presence of a laser aiming beam in the instrument, which is presently true only of therapeutic laser instruments. However, in principle it is possible to incorporate a laser aiming beam within the intraocular shaft of any type of instrument for any type of intervention. We are presently working to incorporate aiming beams into instruments for non-laser retinal operations.

We also proposed virtual fixtures to aid membrane peeling using Micron. The success of these fixtures in reducing applied force during engaging and lifting of the membrane was demonstrated on an artificial phantom and it was shown that both the downward engaging force and upward peeling forces decreased by significant amounts. Future work will involve experimenting with different motion scaling scales, zones, and hard stop limits to find the optimum parameters for the process. We would also like to eventually carry out peeling experiments with Micron in live animals. In that case, we have to incorporate our real time plane estimation algorithm to get an accurate position of the retina at all times. Real time plane estimation may lead to dynamic changes in the motion scaling and hard stop zones, in which case we have to come up with new algorithms for smooth motion of the Micron tool-tip in these zones.

List of Figures

1.1 Exploded view of Micron 4

1.2 Schematic diagram showing Micron and all associated systems 5

1.3 Micron system setup, showing Micron handheld vitreoretinal surgical instrument, ASAP optical tracker, stereo operating microscope, and cameras. 6

1.4 Schematic diagram showing ray paths (P_1 to P_5) in the eye [28]. The ray paths, also called "isopixel curves", are shown at fixed steps of 3.5 mm along with their correspondences to pixel distances d_{op} from the optical axis. 10

2.1 Laser interfaced with the Micron end-effector. 14

2.2 Distances of the estimated position of the intersection of the laser beam and the retinal surface from the true phantom plane during the surface tracking experiment. The plot demonstrates that the triangulated beam points are noisy, and hence should be filtered. 16

2.3 Fiducials used for estimation of the true plane during the surface tracking experiment. 18

2.4 Plane displacement along z axis over the surface tracking period. The displacement in the z axis is computed with respect to a stationary point on the initial plane. 19

2.5 Angles of the estimated and true plane normals from the x,y, and z axes during the surface tracking experiment. 20

2.6 The tip reprojection error plotted against the distance of the tip from the initialized plane, which is a measure of the depth of the tip in the saline water. . 22

2.7 Histograms of the signed distances of the linearly triangulated laser points from the phantom plane with, and without error calibration 24

3.1 Scanning a laser interfaced with the micron end effector in a circle results in an ellipse projected onto the the retinal surface 26
3.2 Variables used in the structured light method 28
3.3 Phantom used for the membrane peeling experiment 30
3.4 Distance of the actual and null tip positions from the estimated retinal surface during trial. 31

List of Tables

2.1 Table summarizing the signed distances d in microns of the computed 3D Laser points from the actual phantom plane with different error calibrations . 23

Bibliography

[1] Roizenblatt, M., Edwards, T. L. & Gehlbach, P. L. Robot-assisted vitreoretinal surgery: current perspectives. *Robotic surgery (Auckland)* **5**, 1 (2018).

[2] Almony, A. *et al.* Techniques, rationale, and outcomes of internal limiting membrane peeling. *Retina* **32**, 877–891 (2012).

[3] Yang, S., MacLachlan, R. A. & Riviere, C. N. Manipulator design and operation of a six-degree-of-freedom handheld tremor-canceling microsurgical instrument. *IEEE/ASME Trans. Mechatron.* **20**, 761–772 (2015).

[4] Yang, S., Martel, J. N., Lobes Jr, L. A. & Riviere, C. N. Techniques for robot-aided intraocular surgery using monocular vision. *Int. J. Robotics Research* **37**, 931–952 (2018).

[5] Klein, R., Klein, B., Wang, Q. & Moss, S. E. The epidemiology of epiretinal membranes. *Transactions of the American Ophthalmological Society* **92**, 403 (1994).

[6] Mitchell, P., Smith, W., Chey, T., Wang, J. J. & Chang, A. Prevalence and associations of epiretinal membranes: the blue mountains eye study, australia. *Ophthalmology* **104**, 1033–1040 (1997).

[7] Foos, R. Vitreoretinal juncture; epiretinal membranes and vitreous. *Investigative ophthalmology & visual science* **16**, 416–422 (1977).

[8] Sebag, J. Anomalous posterior vitreous detachment: a unifying concept in vitreo-retinal disease. *Graefe's archive for clinical and experimental ophthalmology* **242**, 690–698 (2004).

[9] Brooks Jr, H. L. Macular hole surgery with and without internal limiting membrane peeling. *Ophthalmology* **107**, 1939–1948 (2000).

[10] Gupta, P. K., Jensen, P. S. & de Juan, E. Surgical forces and tactile perception during retinal microsurgery. In *International Conference on Medical Image Computing and Computer-Assisted Intervention*, 1218–1225 (Springer, 1999).

[11] Jagtap, A. D. & Riviere, C. N. Applied force during vitreoretinal microsurgery with handheld instruments. In *The 26th Annual International Conference of the IEEE Engineering in Medicine and Biology Society*, vol. 1, 2771–2773 (IEEE, 2004).

[12] Singh, S. & Riviere, C. Physiological tremor amplitude during retinal microsurgery. In *Proceedings of the IEEE 28th Annual Northeast Bioengineering Conference (IEEE Cat. No. 02CH37342)*, 171–172 (IEEE, 2002).

[13] Kadonosono, K. *et al.* Endovascular cannulation with a microneedle for central retinal vein occlusion. *JAMA Ophthalmology* **131**, 783–786 (2013).

[14] Taylor, R. *et al.* A steady-hand robotic system for microsurgical augmentation. *The International Journal of Robotics Research* **18**, 1201–1210 (1999).

[15] Gonenc, B., Handa, J., Gehlbach, P., Taylor, R. H. & Iordachita, I. Design of 3-dof force sensing micro-forceps for robot assisted vitreoretinal surgery. In *2013 35th Annual International Conference of the IEEE Engineering in Medicine and Biology Society (EMBC)*, 5686–5689 (IEEE, 2013).

[16] Edwards, T. L. *et al.* First-in-human study of the safety and viability of intraocular robotic surgery. *Nature Biomedical Engineering* **2018**, 649–656 (2018).

[17] Kummer, M. P. *et al.* Octomag: An electromagnetic system for 5-dof wireless micromanipulation. *IEEE Transactions on Robotics* **26**, 1006–1017 (2010).

[18] MacLachlan, R. A. & Riviere, C. N. High-speed microscale optical tracking using digital frequency-domain multiplexing. *IEEE Trans. Instrum. Meas.* **58**, 1991–2001 (2009).

[19] Yang, S. *et al.* Optical coherence tomography scanning with a handheld vitreoretinal micromanipulator. In *2012 Annual International Conference of the IEEE Engineering in Medicine and Biology Society*, 948–951 (IEEE, 2012).

[20] Yang, S., MacLachlan, R. A. & Riviere, C. N. Toward automated intraocular laser surgery using a handheld micromanipulator. In *2014 IEEE/RSJ International Conference on Intelligent Robots and Systems*, 1302–1307 (IEEE, 2014).

[21] Mukherjee, S. *et al.* Toward monocular camera-guided retinal vein cannulation with an actively stabilized handheld robot. In *Robotics and Automation (ICRA), 2017 IEEE International Conference on*, 2951–2956 (IEEE, 2017).

[22] He, X., Gehlbach, P., Handa, J., Taylor, R. & Iordachita, I. Toward robotically assisted membrane peeling with 3-dof distal force sensing in retinal microsurgery. In *2014 36th Annual International Conference of the IEEE Engineering in Medicine and Biology Society*, 6859–6863 (IEEE, 2014).

[23] Becker, B. C., MacLachlan, R. A., Lobes Jr., L. A., Hager, G. D. & Riviere, C. N. Vision-based control of a handheld surgical micromanipulator with virtual fixtures. *IEEE Trans. Robot.* **29**, 674–683 (2013).

[24] MacLachlan, R. A. *et al.* Micron: an actively stabilized handheld tool for microsurgery. *IEEE Transactions on Robotics* **28**, 195–212 (2011).

[25] Tayama, T. *et al.* Image processing for autonomous positioning of eye surgery robot in micro-cannulation. *Procedia CIRP* **65**, 105–109 (2017).

[26] Bergeles, C., Shamaei, K., Abbott, J. J. & Nelson, B. J. Single-camera focus-based localization of intraocular devices. *IEEE Trans. Biomed. Eng.* **57**, 2064–2074 (2010).

[27] Mccannel, C. A. *et al.* Snoring is associated with unexpected patient head movement during monitored anesthesia care vitreoretinal surgery. *Retina* **32**, 1324–1327 (2012).

[28] Bergeles, C., Kratochvil, B. E. & Nelson, B. J. Visually servoing magnetic intraocular microdevices. *IEEE Transactions on Robotics* **28**, 798–809 (2012).

[29] Mukherjee, S., MacLachlan, R. & Riviere, C. Velocity-limiting control of an active handheld micromanipulator. *Journal of medical devices* **10**, 030944 (2016).

[30] Braun, D., Yang, S., Martel, J. N., Riviere, C. N. & Becker, B. C. EyeSLAM: Real-time simultaneous localization and mapping of retinal vessels during intraocular microsurgery. *International Journal of Medical Robotics and Computer Assisted Surgery* **14**, e1848 (2018).